

Comparison of low-order aerodynamic models and RANS CFD for full scale 3D vertical axis wind turbines

P.-L. Delafin*, T. Nishino, A. Kolios, L. Wang

Centre for Offshore Renewable Energy Engineering, Cranfield University, Cranfield, MK43 0AL, UK

Abstract

A Double Multiple Streamtube model, a free-wake vortex model (both widely used for vertical axis wind turbine design) and RANS CFD simulations are used in this work to predict the performance of the 17m Vertical Axis Wind Turbine, field tested by Sandia National Laboratories. The three-dimensional, full scale calculations are compared with the experiments in terms of power coefficient, power and instantaneous turbine torque to assess the validity of each model. Additionally, the two aerodynamic models and RANS CFD are compared to each other in terms of thrust and lateral force. The two models and CFD agree well with the experiments at the turbine optimal tip speed ratio. However, away from the optimal tip speed ratio, the streamtube model significantly deviates from the experimental data and from the other numerical models. RANS CFD gives a good agreement with the experiments, slightly underestimating the power coefficient at every tip speed ratio tested. The vortex model proves to be a useful tool with a better accuracy than the streamtube model and a much lower computational cost compared to RANS CFD.

Keywords: Double Multiple Streamtube, Free-wake vortex, 3D Computational Fluid Dynamics, Darrieus turbine, Instantaneous torque

1. Introduction

There was a large interest in Vertical Axis Wind Turbines (VAWT's) in the 1970's [1, 2] before the wind energy industry was dominated by Horizontal Axis Wind Turbines (HAWT's). Although

*Corresponding author

Email address: pierreluc.delafin@gmail.com (P.-L. Delafin)

slightly less efficient than the conventional HAWT's, VAWT's have several notable advantages [3], for example: (1) they are insensitive to the wind direction; (2) it is possible to install the drive train close to the ground; and (3) they have a lower center of gravity compared to HAWT's. Additionally, the size of large scale offshore HAWT's is limited by the fatigue cycles experienced by the blades during each revolution due to the gravitational loads. VAWT's overcome this problem since the gravitational loads always apply a constant stress on the blades. The scalability of VAWT's is therefore superior to HAWT's. For these reasons, there has recently been a resurgent interest in VAWT's, especially for urban [4] and offshore [5, 6, 7] applications.

Although mechanically simpler than HAWT's (as there is no need of yawing system and usually no pitching mechanism for the blades), the aerodynamics of VAWT's is more complicated due to the continuously varying angle of attack seen by the blades. This can lead to dynamic stall at a low tip speed ratio (TSR). Furthermore, the wake of the blades in the upstream half of the turbine interacts with the blades traveling through the downstream half.

Numerical models of different complexity have been developed to predict the aerodynamic performance of VAWT's. These models can be divided into three main categories: streamtube models, vortex methods and Computational Fluid Dynamics (CFD). Streamtube models, based on the principle of momentum conservation in a quasi-steady flow, were first developed in the 1970's [2, 8]. They are still widely used for VAWT's design and have benefited from several improvements to the initial models [9, 10]. However, nowadays streamtube models receive some criticisms regarding the accuracy of their results, i.e. good agreement with experiments could result from cancellation of errors [11]. Vortex methods were developed slightly later than streamtube models [12] and are still an active research topic [13, 14]. Their unsteady formulation and explicit wake modeling often lead to a better accuracy compared to streamtube models. More recently, CFD simulations have been widely used to predict the performance of VAWT's, such as 2D RANS simulations [15, 16, 17], 3D RANS simulations [18, 19, 20], and 2.5D Large-Eddy Simulations (LES) [21, 22]. CFD has proven to be a useful tool to predict the turbine performance, instantaneous forces and the flow field around the turbine. CFD is however much more time consuming than vortex methods and streamtube models.

The aforementioned studies focus on small scale wind turbines to compare the numerical re-

sults with wind or water tunnel measurements. The aim of the present study is to compare stream-tube models, vortex methods and CFD with existing experiments for a 3D full scale VAWT. Both averaged (power, power coefficient) and instantaneous data (turbine torque) are used to assess the validity of each model at three different TSR, covering the operating range of VAWT's. The study focuses on the comparison of different computational models for the full scale turbine used in the experiments (in an isolated configuration). We do not attempt to improve the turbine design or investigate the interaction of multiple turbines in this study as these are outside the scope of the study.

2. Wind turbine and test conditions

Experimental data for full scale VAWT's, with sufficient information for a detailed comparison with aerodynamic models, are limited. For example, experiments on a 12 kW VAWT have been carried out at Uppsala University [23] but the tangential force measurements were distorted by the dynamics of the turbine [24]. Thus, the wind turbine used in this study is the second version of the 17m-diameter (D) VAWT tested by Sandia National Laboratories in the 1980's (Fig. 1). It is a 2-bladed Φ -shape VAWT with a 0.51m diameter central tower and no strut. Blades are divided into 3 sections (straight/circular/straight) approximating a Troposkein shape. The aerodynamic cross section is a NACA 0015 with a 0.61m chord length (c). The turbine swept area (A_S) is 187m² and the ground clearance is 4.88m. Wind speeds are given at the turbine mid height (13.5m from the ground) assuming a velocity profile based on the power law (Eq. 1) to model the effect of wind shear. U_∞ corresponds to the upstream wind speed used to calculate the tip speed ratio, z is the height above ground, Z_{ref} corresponds to the mid height of the turbine and the exponent a equals 0.1 as mentioned in [25]. The density of air is 1 kg/m³, corresponding to a normal day at the test facility (located at a high altitude). In the present study, all calculations take into account the effect of wind shear and the air density measured at the test facility. The solidity of the turbine is 0.16, as calculated by Eq. 2 (N is the number of blades and L is the blade length). More detailed information can be found in the Sandia technical reports [25, 26]. The coordinate frame related to the turbine used in this study is presented in Fig. 2.

$$U_x(z) = U_\infty \times \left(\frac{z}{Z_{\text{ref}}}\right)^a \quad (1)$$

$$\sigma = \frac{NcL}{A_S} \quad (2)$$



Figure 1: Sandia National Laboratories 17m VAWT [27].

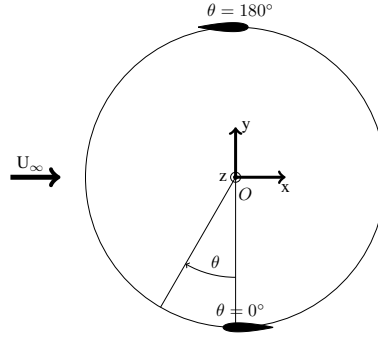


Figure 2: Coordinate frame, view from the top of the turbine.

80 Extensive measurements have been reported on this turbine which makes it a good reference
 81 for comparison with numerical models. Averaged power, power coefficient and especially the
 82 instantaneous turbine torque have been measured [27]. The instantaneous turbine torque provides
 83 information about the aerodynamic phenomena occurring during the turbine revolution, which is
 84 very useful for the validation of numerical models.

85 The turbine was operated experimentally at rotational speeds ranging from 29.8rpm to 54.8rpm.
 86 This study focuses on the speed 38.7rpm at which torque measurements are available from TSR =

2 to $TSR = 8$. This allows comparisons with numerical models for a wide range of conditions, including two extreme cases where blades are experiencing dynamic stall ($TSR = 2$) and when the induction is high ($TSR = 8$).

3. Numerical models

3.1. *TM4E: Turbine Model version 4E*

TM4E [10] is based on Paraschivoiu's Double Multiple Streamtube model [9]. The flow through the turbine's swept volume is divided into a series of streamtubes and then induced velocities are calculated separately over upwind and downwind half-cycles of the rotor. TM4E averages momentum losses created by all elements over lateral streamtubes for each half-cycle. This modification was considered necessary for complex rotor shapes and enables the code to be used for various types of turbine geometries (Φ -shape, H-shape, V-shape, etc). The upwind and downwind halves of the rotor are thus automatically divided into 200 horizontal layers for the calculation of the induced velocities.

TM4E was developed to take into account 3D effects like tip losses, junction losses, tower wake, wind shear as well as dynamic stall effects through the Gormont model [28]. The Gormont model was enhanced in TM4E using corrections proposed by Masse [29] and Berg [30]. A Masse coefficient $A_M = 6$, known to give good results for the SNL 17m VAWT [30], is used in this study.

3.2. *CACTUS: Code for Axial and Cross-flow TURbine Simulation*

CACTUS is a three-dimensional free-vortex code using the lifting line approximation to model the blades [13]. Each blade is discretized into a number of blade elements containing a bound vortex line. The wake is represented by a time-dependent vortex lattice. At each time step, each blade element produces a new shed vortex line segment connected to the bound vortex by two trailing vortex line segments. The velocity field induced by the entire vortex system is calculated using the Biot-Savart law.

The calculations performed in this study take into account the wind shear and use the Leishman-Beddoes dynamic stall model [31, 32].

Following the results of a convergence study, each blade is represented by 27 elements and 40 time

steps are used per revolution. Calculations are run for a number of turbine revolutions which leads to a good level of convergence (difference of the power coefficient CP is less than 0.7% between the last two revolutions). The number of turbine revolutions required varies from 5 (low TSR) to 20 (high TSR).

3.3. CFX

3.3.1. Mesh and boundary conditions

The computational domain (Fig. 3) is meshed with a structured grid and is divided into two parts:

- An outer domain of length $60 D$, width $60 D$ and height $11 D$. This domain contains 2×10^6 cells (gray part in Fig. 3).
- A rotating cylindrical domain containing the turbine (green part in Fig. 3). The rotor domain has a diameter of $3D$ and a height of $1.1D$ (19 m). It contains 7×10^6 cells.

A transient rotor/stator interface using the GGI (General Grid Interface) method is employed between the rotor and the stator. Figure 4 shows the mesh around the turbine in the equatorial plane. Figure 5 shows a close view of the mesh around one blade in the equatorial plane. The mesh has been refined close to the blades to reach $y^+ \sim 1$ in order to resolve the viscous sublayer sufficiently. This leads to a y^+ independent solution, as discussed in [15]. A blade cross-section is represented by 140 nodes in the chordwise direction. 145 nodes are used in the spanwise direction for each blade.

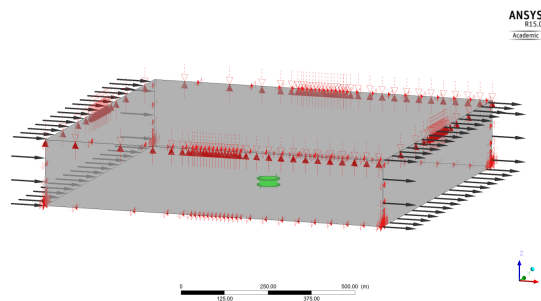


Figure 3: Computational domain including the rotor (green part) and the stator (gray part).

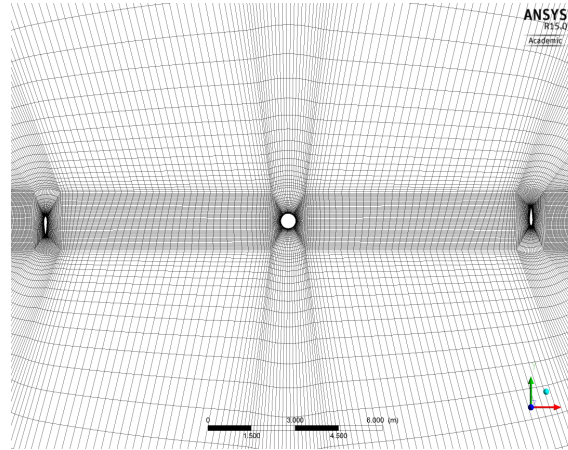


Figure 4: Close view of the structured mesh in the equatorial plane.

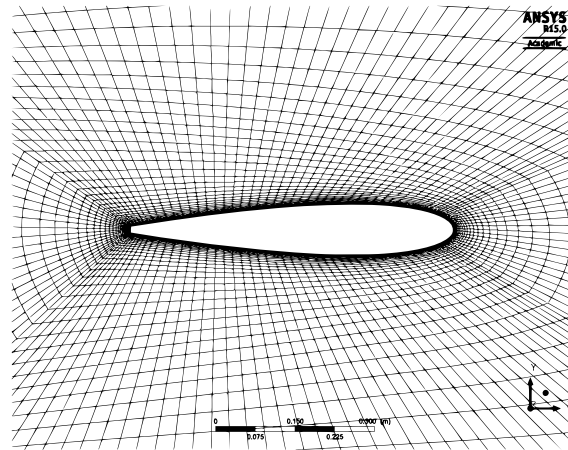


Figure 5: Close view of the mesh around the airfoil.

133 The inlet velocity is defined at the inlet boundary using a power law to take into account the
 134 effect of wind shear in the calculations. It was verified in the results that the inlet velocity profile
 135 is maintained in the computational domain, especially in front of the turbine. The inlet turbulence
 136 intensity is set to 10% with a viscosity ratio $\mu_t/\mu = 100$. This leads, after decaying between the
 137 upstream boundary and the turbine (despite the presence of a wind shear) to a turbulence intensity
 138 of 0.12% around the turbine. This low turbulence intensity is not representative of the turbulence
 139 of the real wind but it should not affect significantly the prediction of flow around the blades. At
 140 the center of the turbine, the turbulence intensity ranges between 1% and 15% due to the wakes
 141 generated by the blades and the tower. The bottom boundary is set as wall to maintain the wind

shear. The lateral and top boundaries are set as symmetry boundaries. An outlet condition with 0 Pa relative static pressure is imposed on the downstream boundary. Finally, blades and tower are set as solid walls.

The time step used in the calculations always corresponds to a variation of the azimuthal angle of the turbine $\Delta\theta = 1^\circ$. The number of revolutions necessary to reach a periodic state depends on the tip speed ratio. As presented in Tab. 1, this number varies from 3 revolutions at $TSR = 2.02$ to 20 revolutions at $TSR = 7.98$. The lower the tip speed ratio the faster the wake develops behind the turbine since the calculations, as with the experiments in this case, employ a constant rotational speed and a variable wind speed. Table 1 also indicates the maximum value of y^+ reached on the blades during one revolution. These values range from 2.1 to 2.5 which satisfies the requirements of the $k-\omega$ SST turbulence model used.

TSR	Number of revolutions	Variation of CP between last 2 revolutions	Max y^+
2.02	3	+0.12%	2.5
4.6	5	-1.07%	2.4
7.98	20	-1.50%	2.1

Table 1: Summary of CFD convergence and y^+ .

3.3.2. Turbulence models and numerical procedure

Incompressible Unsteady Reynolds-Averaged Navier-Stokes (URANS) equations are solved using ANSYS CFX [33]. The $k-\omega$ SST (Shear Stress Transport) turbulence model [34] is used to model the Reynolds stress. This turbulence model blends the $k-\omega$ and $k-\epsilon$ turbulence models to benefit from the accuracy of the ω -formulation in the boundary layer, especially in presence of flows with adverse pressure gradients, and the insensitivity of the ϵ -formulation to the freestream boundary conditions. It is therefore known to be suitable for lifting bodies applications when used with a mesh satisfying the criteria $y^+ \sim 1$ [35]. It was shown to be one of the best RANS turbulence models for Darrieus wind turbines applications [36].

Additionally, the $\gamma - \text{Re}_\theta$ transition model [37] coupled with the $k-\omega$ SST turbulence model (referred to as SST-TM henceforth) has been used at the lowest tip speed ratio. Taking the laminar-turbulent transition into account in RANS calculations improves the accuracy of the lift and drag coefficients predictions in presence of transition effects [38, 39] and improves the modeling of the dynamic stall [40]. It has also been shown to improve the results of VAWT calculations at low tip speed ratios [16], where blades experience dynamic stall. The $\gamma - \text{Re}_\theta$ transition model is based on empirical correlations for the momentum thickness Reynolds number at transition Re_{θ_t} . It uses two additional transport equations: one for Re_{θ_t} which takes non-local empirical correlations and transforms them into a local quantity that can be used in the second equation for γ , the intermittency. γ is used to activate the production term of the turbulence kinetic energy (k) transport equation where the transition criteria are satisfied. Details of the $\gamma - \text{Re}_\theta$ transition model can be found in [37].

Advection terms are discretized using a hybrid first/second order scheme (“High Resolution” scheme in CFX) and the temporal discretization is achieved by using the implicit second order backward Euler scheme. Calculations are run in double precision and are parallelized on 32 CPUs. The computational time required to simulate one turbine revolution is about one day.

4. Validation - pitching airfoil case

A validation study is carried out to assess the accuracy of the ‘relatively low’ mesh resolution used around the blades of the full scale wind turbine (see Section 3.3.1). A pitching airfoil case with dynamic stall is selected because it is close to the complicated flow around a VAWT blade. The experimental work of Lee and Gerontakos [41] is chosen for comparison since it employs a NACA 0012 airfoil, similar to the NACA 0015 airfoil used for the wind turbine, Reynolds number is $\text{Re} = 1.35 \times 10^5$ which is high enough to be relevant to the current VAWT study and the pitching frequency is also relevant to VAWT applications. The pitching axis is located at quarter-chord and the pitching law is given in Eq. 3. The airfoil angle of attack starts from an initial value 10° and pitches between -5° and 25° . It reaches values well beyond the static stall angle, which is around 12° at this Reynolds number [41]. The circular frequency of the oscillations, ω , related to the

189 oscillation frequency f_0 , is defined via the reduced frequency κ (Eq. 4). We choose $\kappa = 0.1$ since it
 190 corresponds to a high pitching rate that covers most of the operating points of the studied VAWT.

$$\alpha(t) = 10^\circ + 15^\circ \sin(\omega t), \quad \omega = 2\pi f_0 \quad (3)$$

$$\kappa = \omega c / 2U_\infty \quad (4)$$

191 The computational domain is two-dimensional and circular with a radius of 50 chords (Fig. 6,
 192 left). The mesh is structured. The coarsest mesh (18k cells) has the same nodes distribution on
 193 the airfoil as on a blade cross section of the full scale wind turbine (140 nodes in the chordwise
 194 direction). The grid spacing in the wall-normal direction is defined to reach $y_{\max}^+ \sim 1$ and to be as
 195 close as possible to that of the wind turbine blades. An O-grid topology is used around the airfoil
 196 (Fig. 6, right). Two finer grids are generated (84k and 170k cells) to compare the 'low resolution'
 197 results with grid converged results. The refinement is done by increasing the number of nodes
 198 in both chordwise and wall-normal directions. The 84k and 170k grids use 440 and 680 nodes,
 199 respectively, in the chordwise direction.

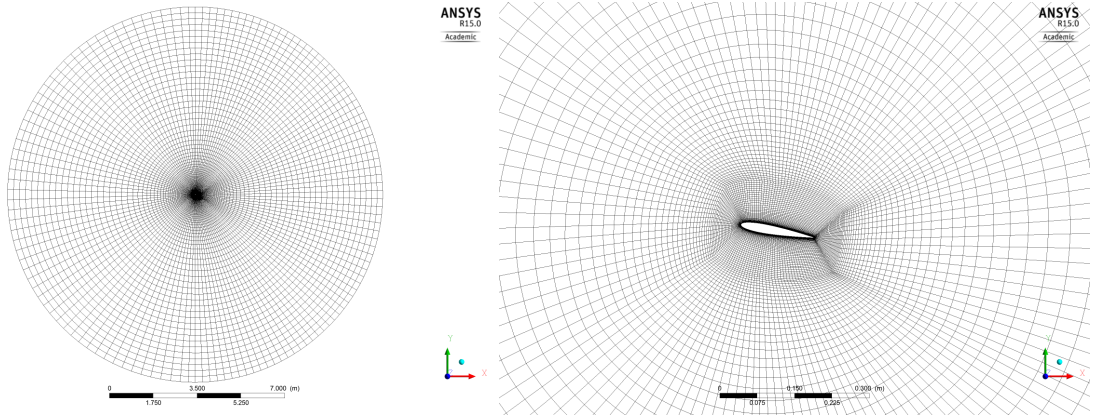


Figure 6: Global view (left) and close view around the airfoil (right) of the mesh for the lowest resolution used (18×10^3 cells).

200 The pitching of the airfoil is achieved by keeping the inlet velocity constant and deforming the
 201 mesh around the airfoil. The initial mesh is generated with the airfoil at an angle of attack of 10° .

Inlet boundary conditions are applied to the left half of the outer boundary (semi-circle) with a constant velocity $U_x = 13.91\text{m/s}$, corresponding to $\text{Re} = 1.35 \times 10^5$ and a turbulence intensity of 5% with $\mu_t/\mu = 10$. The turbulence decays between the inlet boundary and the airfoil to reach a turbulence intensity of 0.25% around the airfoil. This value is close to the experimental value (0.08% at $U_\infty = 35\text{m/s}$). An outlet condition with 0 Pa relative static pressure is imposed on the right half of the outer boundary. Finally, the airfoil is set as a solid wall. Calculations were run with different time step sizes and showed that $\Delta t = 5 \times 10^{-4}\text{s}$ is low enough for the time step independent solution to be obtained for the case studied. This time step corresponds to a maximum CFL value of 160 over a full pitching cycle with the 18k mesh. During most of the cycle, the CFL value is much lower. It should however be noted that for URANS simulations using an implicit scheme for temporal integration, the time step sensitivity is the main criterion to select the time step. The other numerical parameters are the same as mentioned in Section 3.3.2.

The experimental lift and drag coefficients (C_L and C_D) are based on the pressure integration only. C_L and C_D obtained from the CFD simulations are therefore calculated in the same way. Figure 7 presents the results obtained with the three different grids and compares them to the experimental data of Lee and Gerontakos [41]. The three grids give the same C_L and C_D from $\alpha = -5^\circ$ to $\alpha = 15^\circ$ during the upstroke phase. From 15° to 25° , a very small difference can be observed between the 18k grid and the other two on both C_L and C_D curves. All grids predict the peak lift and peak drag coefficients 2° to 3° earlier than the experiment. The main difference between the 18k grid and the other two occurs from 25° to 5° during the downstroke phase. At these angles of attack, the low resolution mesh underestimates the lift and drag coefficients. From 5° to -5° in the downstroke phase, all grids predict the same C_L and C_D again. The results obtained with the SST turbulence model are in agreement with those obtained by Wang et al. [42] at a similar turbulence intensity (0.24%).

Similar comments can be made for the results of the SST-TM model. We can however notice that modeling the transition leads to a slightly better prediction of the peak of lift. Both lift and drag coefficients are also better predicted during the downstroke phase and the hysteresis shown in the experiments around $\text{AoA} = -5^\circ$ is now predicted by the calculations. However, the calculations run in the present study using the SST-TM model do not reach the same level of agreement with

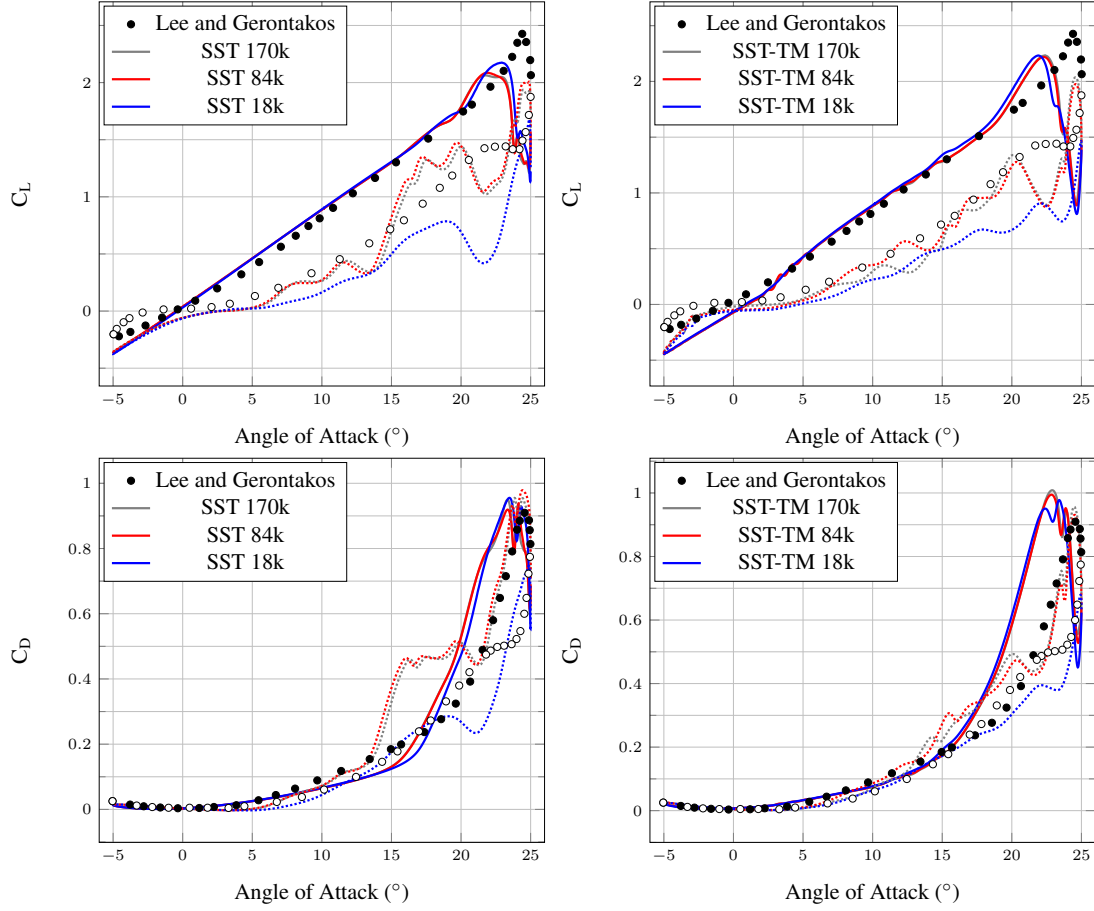


Figure 7: C_L (top) and C_D (bottom) obtained from 2D SST (left) and SST-TM (right) RANS calculations on grids of different refinements. Comparison to experimental data from Lee and Gerontakos [41].

Upstroke: continuous lines and black filled points, Downstroke: dotted lines and white filled points.

$$\text{Re} = 1.35 \times 10^5, c = 0.15\text{m}, \kappa = 0.1$$

the experiments, regarding the peak C_L , as reported by Wang et al. [40]. The beginning of the downstroke phase ($\theta \in [25^\circ, 10^\circ]$) is always difficult to simulate, regardless of the mesh resolution and the turbulence model used [40].

The results presented show that the low mesh resolution used around the blades in the wind turbine calculations gives the same level of accuracy as finer meshes and a good agreement with experiments in the upstroke phase of a pitching airfoil experiencing dynamic stall. The results deviate only during the downstroke phase. When operating at a low tip speed ratio, and therefore experiencing dynamic stall, results will have to be analyzed carefully in the post stall region.

239 However, calculations at higher tip speed ratios should not suffer from the low mesh resolution.

240 5. Results and discussion

241 5.1. Averaged power and power coefficient

242 Figure 8 (left) shows the averaged power calculated by the different numerical models and
 243 compares them with experimental data [27]. The agreement between calculations and experi-
 244 ments is good for all models from 6 m/s to 10 m/s. Deviation from the experiments is only a
 245 few percents at $U_\infty = 7.5$ m/s (Tab. 2). However, at the lowest wind speed ($U_\infty = 4.3$ m/s,
 246 $TSR = 7.98$), low-order models tend to over-predict the output power. CFX gives the best agree-
 247 ment with the experiments, underestimating power by 19%, compared to an overestimation by
 248 231% with CACTUS and 496% with TM4E (Tab. 2). It should be noted that these percentages are
 249 very high because the reference power is very low. The absolute difference in power is only 2.7
 250 kW between experiments and TM4E at $U_\infty = 4.3$ m/s. The agreement between experiments and
 251 calculations is also not very good at high wind speed (low TSR) where the turbine blades experi-
 252 ence dynamic stall. Dynamic stall decreases the aerodynamic performance of the blades, enabling
 253 a natural power control of the turbine. This is why the power reaches a plateau above $U_\infty = 12$ m/s
 254 in the experiments. CACTUS calculations predict this plateau but over-predict the power in this
 255 low TSR range. In contrast, TM4E predicts a decrease of the power above $U_\infty = 12$ m/s leading to
 256 an underestimation of the power. The averaged power predicted by CFX is very close to the one
 257 predicted by TM4E, underestimating the experimental value.

	$U_\infty = 4.3\text{m/s}$ TSR = 7.98	$U_\infty = 7.5\text{m/s}$ TSR = 4.6	$U_\infty = 17.1\text{m/s}$ TSR = 2.02
CFX	-19.2	-3.4	-15.2
CACTUS	+230.7	+5.2	+20.5
TM4E	+496	-0.5	-14.6

Table 2: Deviation of the predicted power from the experiments, in percent (%).

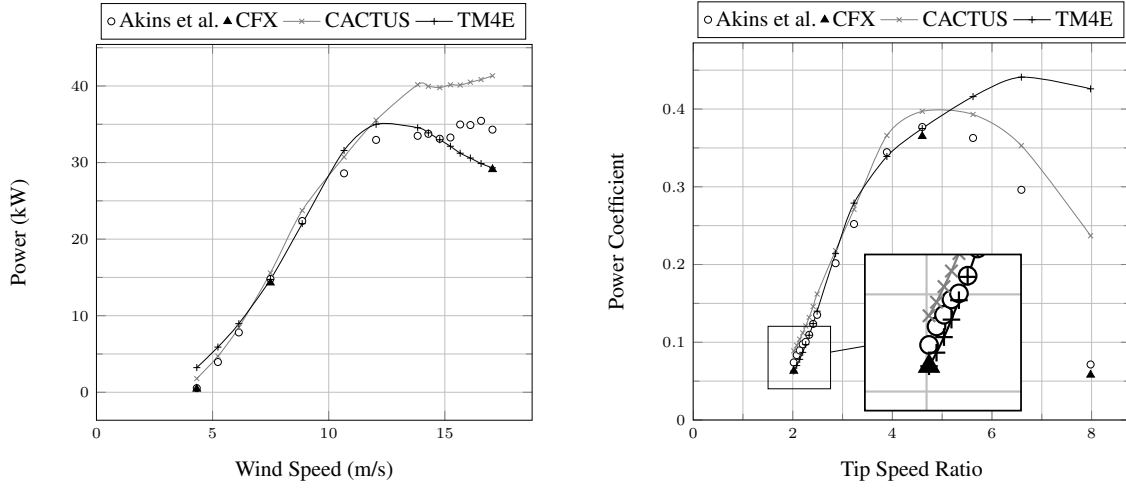


Figure 8: Comparison of power (left) and power coefficient (right) measured by Akins et al. [27] and calculated by TM4E, CACTUS and CFX. $\Omega = 38.7\text{rpm}$

Figure 8 (right) presents the averaged power coefficient (CP) calculated by the different numerical models and compares them with experimental data [27]. The trend of the experimental curve is well predicted by CACTUS and CFX with a prediction of the maximum CP at TSR = 4.6 as in the experiments. However, it can be observed that CACTUS always overestimates the power coefficient (Tab. 2), especially at high TSR. CFX underestimates the CP at every TSR (Tab. 2). TM4E gives good agreement with the experiments from TSR = 2 to 4.6 but does not predict a decrease after TSR = 4.6. The CP predicted by TM4E is therefore significantly over-estimated above TSR = 4.6 and the maximum CP is not predicted at the right TSR.

These comparisons show that the three numerical models used give a fairly good prediction of the power (and CP) obtained at the turbine's optimal tip speed ratio. However, predictions at low and high tip speed ratios do not have the same level of accuracy. At low TSR, the turbine performance is influenced by dynamic stall effects. This 3D, highly unsteady and non-linear phenomenon is very complicated to model which explains the differences observed between experiments and calculations at low TSR. Both TM4E and CACTUS rely on a dynamic stall model (Gormont [28] and Leishman-Beddoes [31], respectively) and CFX relies on the RANS equations, closed by the $k-\omega$ SST turbulence model. The validation study in Section 4 showed that the lift is under-estimated due to the relatively coarse mesh used in this study during the stalled phase.

Using a finer mesh would therefore increase the output power predicted at low TSR and improve the agreement between CFD and experiments, but at a significantly higher computational cost. At high tip speed ratio, the turbine performance is influenced more by viscous effects (friction on blades) and the turbine wake also plays a key role in the power prediction. DMST methods (TM4E) have a poor description of the wake, which can explain its poor prediction at $\text{TSR} = 7.98$. Vortex models (CACTUS) have an inviscid description of the wake through the shedding of vortex elements every time step, which leads to a better accuracy than DMST at high TSR (Fig. 8 (right)). CFD (CFX) accounts for the viscous/turbulence effects by solving the RANS equations, leading to a much better accuracy compared to TM4E and CACTUS at high TSR.

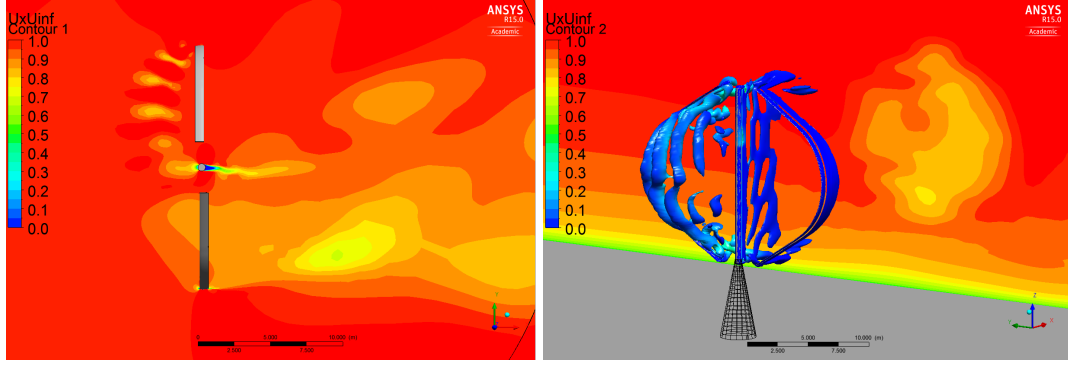
5.2. Flow field

Figure 9 shows the flow field around the turbine, resulting from CFD simulations, at $\text{TSR} = 2.02$ (Fig. 9(a)), $\text{TSR} = 4.6$ (Fig. 9(b)) and $\text{TSR} = 7.98$ (Fig. 9(c)). Blades are at the azimuthal angles $\theta = 0^\circ$ and 180° in all pictures. Pictures on the left show the non dimensional streamwise velocity field (U_x/U_∞) in the equatorial plane. Pictures on the right show iso-surfaces of Q-criterion ($Q = 40 \text{ s}^{-2}$) and also display the non dimensional streamwise velocity in a vertical plane located $1.5 D$ downstream the turbine.

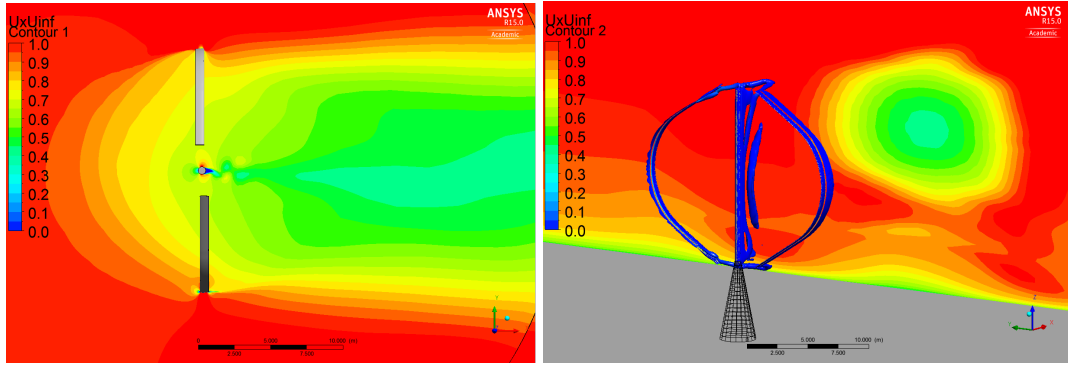
Figure 9(a) shows the vortex shedding occurring during the dynamic stall phase of the blades at $\text{TSR} = 2.02$ ($\theta \in [70^\circ, 180^\circ]$). Vortices are shed in the wake of the blades and convected downstream where they will interact with the blade traveling in the downstream half of the turbine. The wake of the tower can also be observed. As shown in both pictures, the wake of the turbine is not symmetrical at this TSR. The flow is slower behind the half of the turbine where blades do not experience dynamic stall ($\theta \in [0^\circ, 70^\circ]$).

Figure 9(b) shows that the wake is almost symmetrical at $\text{TSR} = 4.6$ and that $1.5 D$ downstream the turbine, its shape looks like the shape of the turbine. The iso-surfaces of Q-criterion show only thin layers shed behind the blades, which suggests that the vortices shed from the turbine are much less compared to the low TSR case.

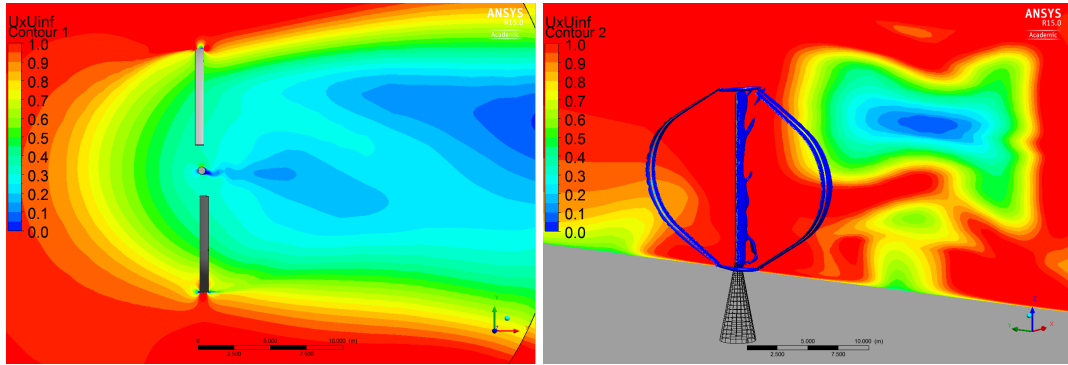
Figure 9(c) shows similar wake patterns to those at $\text{TSR} = 4.6$ in the equatorial plane. However it can be noticed that the flow velocity is further reduced as the tip speed ratio increases: the lowest



(a)



(b)



(c)

Figure 9: Left: Contours of non dimensional velocity U_x/U_∞ in the equatorial plane (the turbine is rotating in the clockwise direction). Right: iso-surfaces of Q -criterion ($Q = 40s^{-2}$) with a plane located $1.5 D$ downstream (25.5m) showing contours of U_x/U_∞ . The conical tower located below the turbine has been added to the figure only for easier visual recognition of the turbine position.

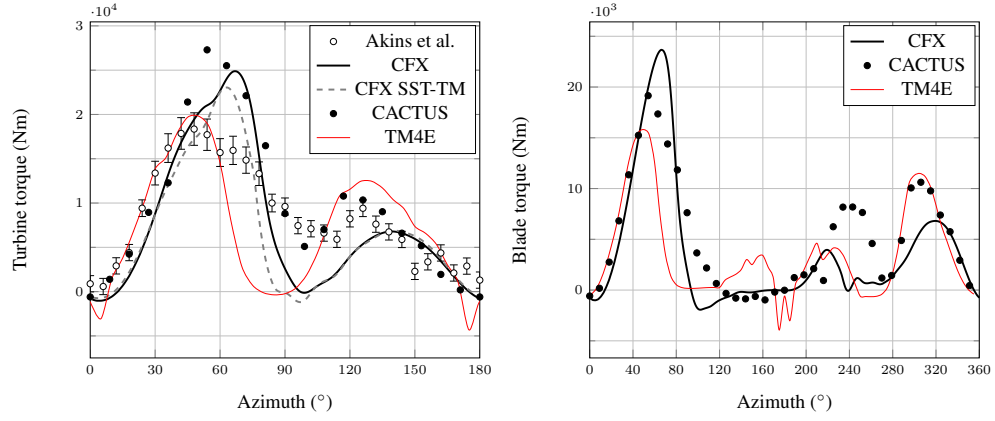
$\Omega = 38.7\text{rpm}$, (a): $\text{TSR} = 2.02$, (b): $\text{TSR} = 4.6$, (c): $\text{TSR} = 7.98$.

velocity in the wake of the turbine is about 40% of the upstream velocity (U_∞) at TSR = 4.6 whereas it is only 20% to 30% at TSR = 7.98. Additionally, the wake observed 1.5 D downstream the turbine has a different shape.

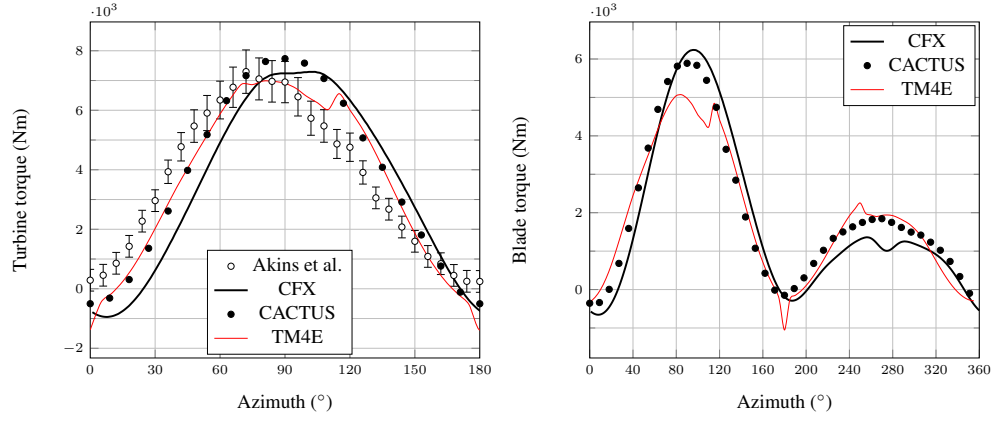
5.3. Instantaneous torque

Comparisons based on the averaged power and power coefficient are important but a good agreement could be obtained without predicting well the instantaneous phenomena, via cancellation of errors for example. To properly design the wind turbine components (blades, drive train, tower, bearings, etc.) it is essential to predict instantaneous aerodynamic forces accurately. This section compares calculations with experiments based on the instantaneous torque. Experimental data are available in term of the turbine torque (torque of the two blades together), measured for half a revolution [27]. In fact, a symmetric behavior of the turbine torque evolution was observed in the experiments for this 2-blade turbine. Figure 10 presents comparisons of the turbine torque (left) between the experiments and calculations as well as comparisons of the torque of one blade (Fig. 10 (right)) for the three numerical models. Measurements have been given with 'an estimate of accuracy of 10% of the reading or 5% of peak torque' [27]. Thus, the maximum of those two values (at a given TSR) is used to plot uncertainty bars in Fig. 10.

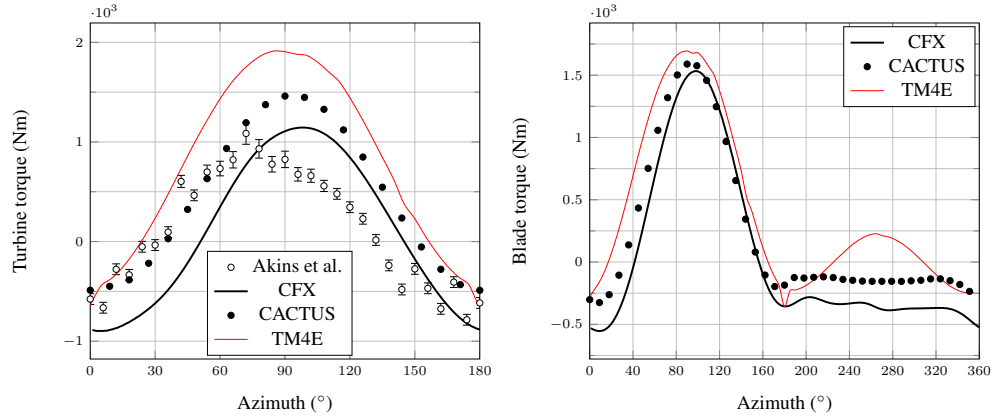
Figure 10(a) (left) shows the turbine torque evolution at TSR = 2.02. The calculations show the same trend as the experiments with the first peak of torque at $\theta \sim 60^\circ$ and the second lower peak at $\theta \sim 120^\circ$. However, the torque amplitude and the exact locations of the peaks vary significantly for the three numerical models. TM4E predicts well the amplitude of the first peak but the torque decreases sharply right after the peak and falls to near zero values, which is not in agreement with the experiments. CACTUS significantly over-predicts the amplitude of the first peak (+48.7%) but then the torque becomes close to the experiments. CFX gives similar results to CACTUS for the first peak. The overestimation of the amplitude is lower (+35.6%) but the peak is delayed by 20° of azimuth. Then, the torque decreases sharply to reach zero around $\theta = 100^\circ$. It increases again to reach the second peak at $\theta = 140^\circ$. Torque values are close to the experiments from $\theta = 140^\circ$ to $\theta = 180^\circ$. Most of the predictions are outside the uncertainty range given in [27]. However, it should be noted that the standard deviation of the measurements, although not given



(a)



(b)



(c)

Figure 10: Comparisons between measurements made by Akina et al. [27] and calculations with TM4E, CACTUS and CFX for the turbine torque (left) and the torque of one blade (right).

$\Omega = 38.7\text{rpm}$, (a): $\text{TSR} = 2.02$, (b): $\text{TSR} = 4.6$, (c): $\text{TSR} = 7.98$.

at this particular rotational speed, is expected to be significant [27].

An additional CFD simulation has been run at this low tip speed ratio with the $\gamma-Re_\theta$ transition model (referred to as SST-TM). As mentioned in Section 3.3.2, taking into account the laminar-turbulent transition was found to improve the results at low tip speed ratio in previous studies [16] by improving the prediction of the dynamic stall. In the present case, the SST-TM calculation deviates from the original calculation from $\theta = 40^\circ$ to $\theta = 100^\circ$. The maximum torque is lower than in the original calculation (+25.6% compared to the experiment) and is predicted 15° later than in the experiment. The sharp decrease of the torque is similar to the original calculation but occurs earlier, leading to a lower averaged torque. The resulting power is therefore lower than the original case, i.e. using a transition model does not improve the result for the present low tip speed ratio case. It should however be noted that the relatively low mesh refinement used in this study does not allow to achieve full potential of the transition model.

Figure 10(a) (right) shows the instantaneous torque of one blade plotted for a full revolution. The torque in the downstream half of the turbine is lower than in the upstream half since the flow has been slowed down by the blades in the upstream half. The wind speed at the center of the turbine is lower, meaning that both relative wind speed magnitude and blades' angle of attack are lower in the downstream half than in the upstream half. This explains why less torque is produced. However, significant differences can be observed between the three numerical models. The first peak of torque, occurring at $\theta \sim 60^\circ$, is predicted higher with CFX than with CACTUS and TM4E. This first peak is also predicted at different azimuth with the different models. The blade is thus predicted to stall at $\theta = 50^\circ$ with TM4E, $\theta = 54^\circ$ with CACTUS and $\theta = 66^\circ$ with CFX. A deep stall is predicted with CFX as can be seen from the very sharp decrease of torque right after the stall. TM4E and CACTUS present a slightly lighter stall. Also, the three calculations predict two peaks of torque in the second half of the revolution. CACTUS predicts two peaks of similar value (half the peak value of the upstream half). CFX predicts two peaks of lower amplitude compared to CACTUS. TM4E predicts the first peak with a similar amplitude to CFX and the second peak with a similar amplitude to CACTUS. All numerical models predict a very low torque around $\theta = 270^\circ$. The wide range of azimuth at which the torque is low in CFX seems to indicate that this is not only due to the wake of the tower.

Figure 10(b) (left) presents the turbine torque at $TSR = 4.6$. The evolution of the torque is much simpler than at $TSR = 2.02$ since the higher TSR leads to lower angles of attack for the blades and therefore they do not experience stall during the rotation. All calculations reproduce fairly well the experiments. However, the torque predicted by the calculations is shifted toward higher azimuthal angles ($+9^\circ$ for CACTUS and TM4E and $+17^\circ$ for CFX). It should be noted that torque measurements are given with a $\pm 6^\circ$ accuracy 'at best' for the azimuthal angle [27]. The maximum torque is well predicted with CFX, slightly overestimated with CACTUS and slightly underestimated with TM4E. All predictions of the maximum torque fall within the uncertainty range of the measurements but the minimum torque is slightly under predicted. Figure 10(b) (right) compares the torque of one blade computed by TM4E, CACTUS and CFX. The three models predict a high peak of torque in the upstream half and a lower peak of torque in the downstream half. CFX predicts a slightly higher torque than CACTUS in the first half and a slightly lower torque in the second half. TM4E predicts strange secondary peaks at $\theta = 110^\circ$, $\theta = 180^\circ$ and $\theta = 250^\circ$ that may be due to the dynamic stall model. TM4E also predicts a lower torque for the first peak compared to CFX and CACTUS. CFX shows a small decrease of the torque around $\theta = 270^\circ$ that is due to the wake of the tower, as seen in Fig. 9(b). This phenomenon is responsible for the plateau observed in the turbine torque in both CFX and the experimental curves (Fig. 10(b) (left)). Although taking the wake of the tower into account, TM4E and CACTUS do not capture this phenomenon.

Figure 10(c) (left) shows the turbine torque at $TSR = 7.98$. The torque evolution is similar to the one observed at $TSR = 4.6$ but the maximum torque reached is much lower at $TSR = 7.98$. The predictions of TM4E, CACTUS and CFX are significantly different at this TSR. TM4E predicts the peak torque 76% higher than the experimental one. CACTUS calculations are in good agreement with the experiments from $\theta = 0^\circ$ to $\theta = 60^\circ$ but significantly overestimate the torque beyond; the peak torque is 32% higher than the experimental one. CFX gives the best prediction regarding the torque amplitude: the peak torque is only 6% higher than the experimental one (which is within the range of the measurement uncertainty). However, the torque calculated by CFX is shifted by 18° toward the higher azimuthal angles compared to the experiments. Figure 10(c) (right) compares the torque of one blade computed at $TSR = 7.98$. From $\theta = 0^\circ$ to $\theta = 90^\circ$, TM4E

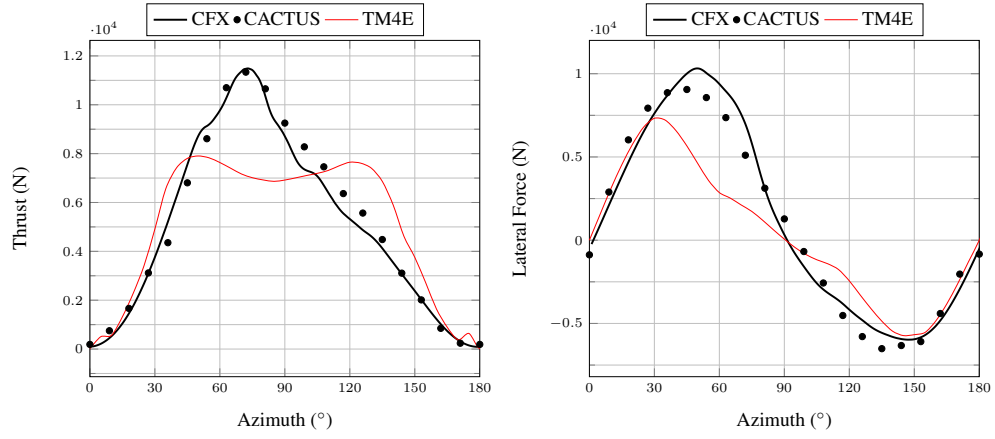
predicts a higher torque than CACTUS, which predicts a higher torque than CFX. From $\theta = 90^\circ$ to $\theta = 180^\circ$, the agreement between the three models is good. The main differences are observed in the downstream half of the turbine: the torque predicted by TM4E reaches positive values while CACTUS and CFX predict an almost constant negative torque. The torque predicted by CFX is lower. The comparison with the experiments in Figure 10(c) (left) confirms that CFX is more accurate than CACTUS which is more accurate than TM4E.

5.4. Thrust and lateral force

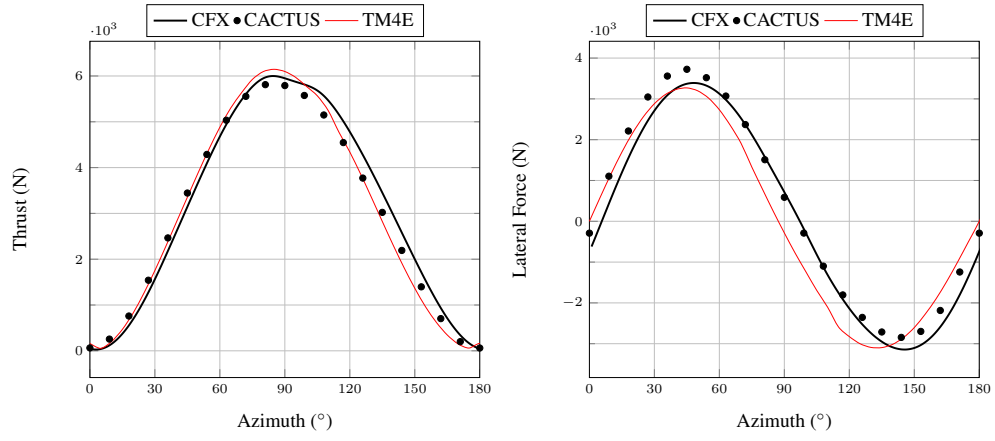
The aim of this section is to compare the predictions of thrust (x direction) and lateral (y direction) forces obtained with the three models used in this study, although no experimental data are available for comparison. These forces are important for the structural design of the turbine (tower, bearings, foundations, etc.). Figure 11 presents the instantaneous thrust force (in the left column) and the instantaneous lateral force (in the right column) at TSR = 2.02 (Fig. 11(a)), TSR = 4.6 (Fig. 11(b)) and TSR = 7.98 (Fig. 11(c)). Results are plotted for half a revolution only because of the symmetric behavior observed for the 2-bladed turbine.

Figure 11(a) (left) shows that CFX and CACTUS predict very similar thrust forces at TSR = 2.02. Both predictions show a single peak of same amplitude, reaching its maximum value at $\theta = 70^\circ$. TM4E however predicts two peaks of lower amplitude at $\theta = 50^\circ$ and $\theta = 125^\circ$. The maximum thrust predicted by TM4E is 30% lower than the one predicted by CACTUS and CFX. Figure 11(a) (right) compares the lateral forces calculated. CFX and CACTUS predict a sinusoidal-like variation of the lateral force. The maximum force calculated by CACTUS is 12% lower than the one calculated by CFX. TM4E deviates from this sinusoidal shape, especially in the first half of the revolution, and predicts a maximum force 29% lower than CFX. The lateral force is in the positive y-direction from $\theta = 0^\circ$ to $\theta = 90^\circ$ and in the negative y direction from $\theta = 90^\circ$ to $\theta = 180^\circ$.

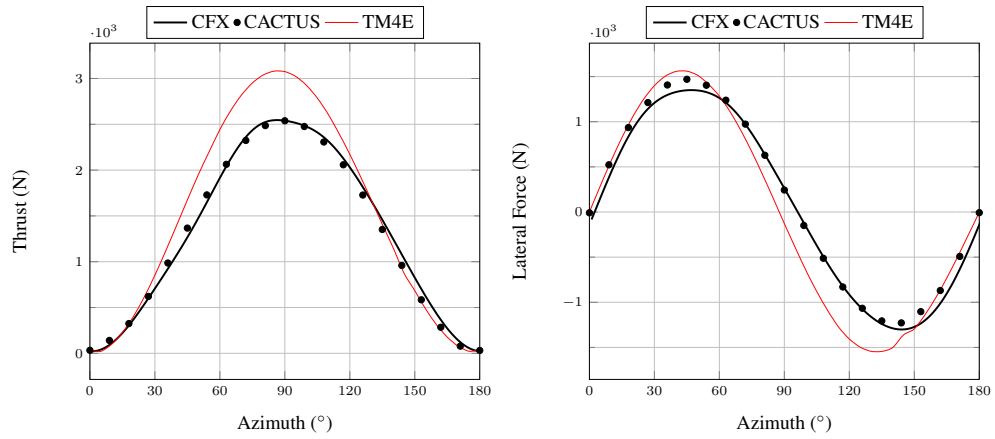
Figure 11(b) (left) shows that all models predict a very similar thrust at the optimal TSR. Figure 11(b) (right) shows that the agreement between the three models is not as good for the lateral force as for the thrust force. The amplitude of the force is very similar for the three models but TM4E results are slightly shifted toward the lower azimuthal angles compared to CACTUS and CFX.



(a)



(b)



(c)

Figure 11: Thrust (left) and lateral force (right), $\Omega = 38.7\text{rpm}$.

(a): $\text{TSR} = 2.02$, (b): $\text{TSR} = 4.6$, (c): $\text{TSR} = 7.98$.

Figure 11(c) (left) indicates that both CACTUS and CFX give a very similar thrust evolution even at the highest TSR (TSR = 7.98). However, TM4E predicts a peak thrust 16% higher than CFX. CFX and CACTUS predictions of the lateral force also agree well at this TSR (Fig. 11(c) (right)) but TM4E deviates from the other results from $\theta = 70^\circ$ to $\theta = 140^\circ$.

These comparisons of thrust and lateral forces show that CFX and CACTUS give very similar results at low, optimal and high TSR. However, TM4E agrees well with the other models only at the optimal TSR and deviates significantly at low and high TSR.

6. Conclusions

A Double Multiple Streamtube model (TM4E), a free Vortex model (CACTUS) and a CFD code (CFX) have been used to compute the instantaneous torque, thrust and lateral forces as well as the averaged power generated by the full scale Sandia 17m Vertical Axis Wind Turbine (second version, unstrutted). The numerical results have been compared with existing experimental data of power and instantaneous torque. The results show that the three methods give very similar results and agree well with the experimental data for the turbine operating at its optimal (medium) tip speed ratio. However, at a high tip speed ratio where friction and wake effects are significant, major differences in power, torque and thrust are observed. CFD leads to the best agreement with the experiments. CACTUS predicts similar thrust and lateral forces to CFX but over-predicts torque and power. TM4E tends to significantly over-predict power, torque and the forces. At a low tip speed ratio, where blades experience dynamic stall, differences between the calculations and experiments as well as between the different numerical models themselves are large. A separate CFD analysis of a pitching airfoil carried out in this study suggested that the CFD results at the low tip speed ratio could be closer to the experiments if the mesh was refined. This would however increase significantly the computational cost for the full scale turbine simulation. It should also be noted that the experimental results themselves contain a certain degree of uncertainties. The comparisons made in this study are thus more qualitative than quantitative.

Overall, the results presented in this paper show that DMST models should be used carefully since they can fail to predict the optimal tip speed ratio and can also overestimate or underestimate turbine torque and thrust forces depending on the operating condition. They are also based on

445 some adjustable parameters (for the dynamic stall model, for example) that have been calibrated
446 for a certain set of experiments. It is therefore difficult to use these models for new shapes of
447 turbines. The free-wake vortex model yielded much better results. Thrust and lateral forces agree
448 well with those predicted by CFD and the agreement with the experimental power and torque is
449 also better than the DMST model. It seems to be a useful method for designing vertical axis wind
450 turbines because of its favorable compromise between accuracy and computational cost. CFD
451 provided the best results at high and medium (optimal) tip speed ratios, at the expense of a high
452 computational cost. Also, CFD can give valuable information about the flow field around the
453 turbine, such as the wake, shed vortices and the deflection of the flow around the turbine. The
454 agreement with experiments at the low tip speed ratio could be improved by refining the mesh,
455 although the dynamic stall is known to be a limitation of RANS CFD and would not be predicted
456 accurately even with a very fine mesh.

457 **7. Acknowledgements**

458 This project has been funded by Aerogenerator Project Limited with the support of the UK
459 Government's Department of Energy & Climate Change.

Nomenclature

Acronyms

AoA	Angle of Attack [°]
CFD	Computational Fluid Dynamics
HAWT's	Horizontal Axis Wind Turbines
LES	Large Eddy Simulation
SST	Shear Stress Transport
TSR	Tip Speed Ratio ($=\Omega R/U_\infty$)
URANS	Unsteady Reynolds-Averaged Navier Stokes
VAWT's	Vertical Axis Wind Turbines

Greek symbols

μ	dynamic viscosity [kg/(m.s)]
μ_t	turbulent dynamic viscosity [kg/(m.s)]
ν	kinematic viscosity [m ² /s]
Ω	turbine rotational speed [rpm]
ρ	density [kg/m ³]
σ	solidity ($=NcL/A_S$)
θ	azimuthal angle [°]

460

Symbols

A_S	turbine swept area [m ²]
c	blade chord length [m]
D	turbine diameter [m]
L	blade length [m]
N	number of blades
P	turbine mechanical power [W]
R	turbine radius [m]
U_x	streamwise wind speed [m/s]
U_∞	free stream velocity [m/s]
y^+	dimensionless wall distance ($=yU_\tau/\nu$)
z	height above ground [m]
Z_{ref}	turbine mid height [m]
C_D	drag coefficient
C_L	lift coefficient
CP	power coefficient ($=P/(0.5 * \rho * A_S * U_\infty^3)$)
Re	chord based Reynolds number ($=U_\infty * c/\nu$)

References

- [1] H. Sutherland, D. Berg, T. Ashwill, A Retrospective of VAWT Technology, Tech. Rep. SAND2012-0304, SANDIA (2012).
- [2] R. Templin, Aerodynamic Performance Theory for the NRC Vertical-Axis Wind Turbine, Tech. Rep. Rept. LTR-LA-160 (1974).
- [3] M. Borg, A. Shires, M. Collu, Offshore floating vertical axis wind turbines, dynamics modelling state of the art. part I: Aerodynamics, *Renewable and Sustainable Energy Reviews* 39 (2014) 1214–1225.
- [4] S. Mertens, Wind energy in urban areas: Concentrator effects for wind turbines close to buildings, *Refocus* 3 (2) (2002) 22–24.
- [5] B. Owens, D. Griffith, Aeroelastic Stability Investigation for Large-Scale Vertical Axis Wind Turbines, *The Science of Making Torque From Wind*, 2014.
- [6] U. Paulsen, H. Madsen, J. Hattel, I. Baran, P. Nielsen, Design Optimization of a 5 MW Floating Offshore Vertical-Axis Wind Turbine, *DeepWind'2013*, 2013.
- [7] A. Shires, Design optimisation of an offshore vertical axis wind turbine, Vol. 166, *ICE-Energy*, 2013, pp. 7–18.
- [8] J. Strickland, The Darrieus Turbine: A Performance Prediction Model Using Multiple Streamtubes, Tech. Rep. SAND75-0431, SANDIA (1975).
- [9] I. Paraschivoiu, Double-Multiple Streamtube Model for Studying Vertical-Axis Wind Turbines, *Journal of Propulsion and Power* (1988) 370–377.
- [10] A. Shires, Development and Evaluation of an Aerodynamic Model for a Novel Vertical Axis Wind Turbine Concept, *Energies* (2013) 2501–2520.
- [11] C. S. Ferreira, H. A. Madsen, M. Barone, B. Roscher, P. Deglaire, I. Arduin, Comparison of Aerodynamic Models for Vertical Axis Wind Turbines, *The Science of Making Torque From Wind*, 2014.
- [12] J. Strickland, B. Webster, T. Nguyen, A vortex model of the Darrieus turbine: an analytical and experimental study, *Journal of Fluids Engineering* 101 (4) (1979) 500–505.
- [13] J. Murray, M. Barone, The Development of CACTUS, a Wind and Marine Turbine Performance Simulation Code, 49th AIAA Aerospace Sciences Meeting, 2011.
- [14] G. Tescione, C. S. Ferreira, G. van Bussel, Analysis of a free vortex wake model for the study of the rotor and near wake flow of a vertical axis wind turbine, *Renewable Energy* 87 (2016) 552–563.
- [15] T. Maître, E. Amet, C. Pellone, Modeling of the flow in a Darrieus water turbine: Wall grid refinement analysis and comparison with experiments, *Renewable Energy* 51 (0) (2013) 497–512.
- [16] J. McNaughton, F. Billard, A. Revell, Turbulence modelling of low Reynolds number flow effects around a vertical axis turbine at a range of tip-speed ratios, *Journal of Fluids and Structures* 47 (0) (2014) 124–138, special Issue on Unsteady Separation in Fluid-Structure Interaction-I.
- [17] B. Paillard, J. Astolfi, F. Hauville, URANSE simulation of an active variable-pitch cross-flow Darrieus tidal

- turbine: Sinusoidal pitch function investigation, *International Journal of Marine Energy* 11 (2015) 9–26.
- [18] E. AMET, Simulation numérique d'une hydrolienne à axe vertical de type Darrieus, Ph.D. thesis, Institut Polytechnique de Grenoble (2009).
- [19] P. Marsh, D. Ranmuthugala, I. Penesis, G. Thomas, Three-dimensional numerical simulations of straight-bladed vertical axis tidal turbines investigating power output, torque ripple and mounting forces, *Renewable Energy* (83) (2015) 67–77.
- [20] A. Orlandi, M. Collu, S. Zanforlin, A. Shires, 3D URANS analysis of a vertical axis wind turbine in skewed flows, *Journal of Wind Engineering and Industrial Aerodynamics* (147) (2015) 77–84.
- [21] C. Simão Ferreira, The near wake of the VAWT: 2D and 3D views of the VAWT aerodynamics, Ph.D. thesis, Ph. D. Dissertation, Delft University of Technology, Delft, The Netherlands, 2009. F. Coton Associate Editor (2009).
- [22] C. Li, S. Zhu, Y.-L. Xu, Y. Xiao, 2.5D large eddy simulation of vertical axis wind turbine in consideration of high angle of attack flow, *Renewable Energy* (51) (2013) 317–330.
- [23] J. Kjellin, F. Bülow, S. Eriksson, P. Deglaire, M. Leijon, H. Bernhoff, Power coefficient measurement on a 12 kW straight bladed vertical axis wind turbine, *Renewable Energy* (36) (2011) 3050–3053.
- [24] M. Rossander, E. Dyachuk, S. Apelfröjd, K. Trolin, A. Goude, H. Bernhoff, S. Eriksson, Evaluation of a Blade Force Measurement System for a Vertical Axis Wind Turbine Using Load Cells, *Energies* (8) (2015) 5973–5996.
- [25] M. Worstell, Aerodynamic Performance of the 17 Meter Diameter Darrieus Wind Turbine, Tech. Rep. SAND78-1737, SANDIA (1978).
- [26] M. Worstell, Aerodynamic Performance of the DOE/Sandia 17-m Diameter Vertical Axis Wind Turbine, *Journal of Energy* (1981) 39–42.
- [27] R. Akins, D. Berg, W. Cyrus, Measurements and Calculations of Aerodynamic Torques for a Vertical-Axis Wind Turbine, Tech. Rep. SAND86-2164, SANDIA (1987).
- [28] R. Gormont, A Mathematical Model of Unsteady Aerodynamics and Radial Flow for Application to Helicopter rotors, Tech. Rep. 72-67, U.S. Army Air Mobility Research and Development Laboratory (1973).
- [29] B. Masse, Description of Two Programs for Calculating Performance and Aerodynamic Loads of a Vertical Axis Wind Turbine, Tech. rep., Institut de recherche de l'Hydro (1981).
- [30] D. Berg, An Improved Double-Multiple Streamtube Model for the Darrieus-Type Vertical Axis Wind Turbine, 6th Biennial Wind Energy Conference and Workshop, 1983, pp. 231–233.
- [31] J. Leishman, Challenges in Modelling the Unsteady Aerodynamics of Wind Turbines, *Wind Energy* 5 (2) (2002) 85–132.
- [32] J. Leishman, T. Beddoes, A Semi-Empirical Method for Dynamic Stall, *Journal of the American Helicopter Society* 34 (1989) 3–17.
- [33] CFX, ANSYS CFX Solver Theory Guide, Vol. 15.0, ANSYS, 2011.

- 529 [34] F. Menter, Two-Equation Eddy-Viscosity Turbulence Models for Engineering Applications, *AIAA Journal* 32 (8)
530 (1994) 1598–1604.
- 531 [35] K. McLaren, S. Tullis, S. Ziada, Computational fluid dynamics simulation of the aerodynamics of a high solidity,
532 small-scale vertical axis wind turbine, *Wind Energy* 15 (3) (2012) 349–361.
- 533 [36] F. Balduzzi, A. Bianchini, R. Maleci, G. Ferrara, L. Ferrari, Critical issues in the CFD simulation of Darrieus
534 wind turbines, *Renewable Energy* 85 (2016) 419–435.
- 535 [37] R. Langtry, F. Menter, Correlation-based transition modeling for unstructured parallelized computational fluid
536 dynamics codes, *AIAA journal* 47 (12) (2009) 2894–2906.
- 537 [38] P. Delafin, F. Deniset, J. Astolfi, Effect of the laminar separation bubble induced transition on the hydrodynamic
538 performance of a hydrofoil, *European Journal of Mechanics-B/Fluids* (2014) 190–200.
- 539 [39] J. N. N. Counsil, K. Goni Boulama, Validating the URANS shear stress transport $\gamma - Re\theta$ model for low-
540 Reynolds-number external aerodynamics, *International Journal for Numerical Methods in Fluids* 69 (8) (2012)
541 1411–1432.
- 542 [40] S. Wang, D. Ingham, L. Ma, M. Pourkashanian, Z. Tao, Turbulence modeling of deep dynamic stall at relatively
543 low Reynolds number, *Journal of Fluids and Structures* 33 (2012) 191–209.
- 544 [41] T. Lee, P. Gerontakos, Investigation of flow over an oscillating airfoil, *Journal of Fluid Mechanics* 512 (2004)
545 313–341.
- 546 [42] S. Wang, D. Ingham, L. Ma, M. Pourkashanian, Z. Tao, Numerical investigations on dynamic stall of low
547 Reynolds number flow around oscillating airfoils, *Computers & Fluids* 39 (9) (2010) 1529–1541.